

Evaluation of Nonhydrostatic Simulations of Northeast Pacific Atmospheric Rivers and Comparison to in Situ Observations

DANIEL L. SWAIN AND BEREKET LEBASSI-HABTEZION

Department of Environmental Earth System Science, Stanford University, Stanford, California

NOAH S. DIFFENBAUGH

Department of Environmental Earth System Science, and Woods Institute for the Environment, Stanford, California

(Manuscript received 7 March 2015, in final form 14 May 2015)

ABSTRACT

Atmospheric rivers are long, narrow bands of concentrated atmospheric water vapor transport that provide an important atmospheric linkage between the subtropics and the midlatitudes, facilitating over 90% of meridional water vapor flux and often resulting in extreme precipitation events in regions of enhanced coastal orography. In this investigation, the authors conduct continuous (3 month), large-domain ($3600 \text{ km} \times 3200 \text{ km}$), high-resolution (4 km), nonhydrostatic simulations using the Weather Research and Forecasting (WRF) Model and compare the observations to previously reported dropsonde observations from the California Land-Falling Jets Experiment (CALJET) and the Pacific Land-Falling Jets Experiment (PACJET) in order to address an existing gap in knowledge regarding the ability of atmospheric models to simulate the finescale vertical and horizontal structure of atmospheric rivers. The WRF simulations reproduce key structural and thermodynamic characteristics of atmospheric rivers—including well-defined corridors of strong water vapor transport, moist-neutral stability in the lower troposphere, and strong low-level jet/water vapor transport maxima near $\sim 1 \text{ km}$ MSL. While WRF does generally capture the extreme values of instantaneous vertically integrated water transport—a defining feature of real-world atmospheric rivers—constituent variables exhibit biases relative to observations, including -11.2% for integrated vapor transport, $+5.9\%$ for integrated water vapor, and -17.7% for 1 km MSL wind speed. Findings suggest that high-resolution nonhydrostatic atmospheric simulations are an appropriate tool for investigating atmospheric rivers in contexts where finescale spatial structure and realistic water vapor transport maxima are important.

1. Introduction

Greater than 90% of all meridional water vapor flux between the subtropics and the midlatitudes occurs within concentrated, filamentary bands known as atmospheric rivers (ARs) (Zhu and Newell 1998). Often thousands of kilometers long but only a few hundred kilometers wide, ARs are transient features at any particular location. They occur throughout midlatitude regions in both hemispheres, and tend to be most prominent over and near ocean basins (Ralph et al. 2004; Bao et al. 2006). When ARs occur in the vicinity of enhanced orography, they can trigger extreme precipitation events and associated flooding (e.g., Neiman et al. 2008a,b; Ralph et al. 2006).

Synoptic-scale transient eddies in the midlatitudes are a primary mechanism by which mass, energy, and momentum are transported poleward between the middle and high latitudes (e.g., Oort 1971). Because transient eddies and ARs can work in concert to dynamically link the earth's low- and high-latitude regions (Neff et al. 2014), changes in the behavior of ARs may have the potential to affect the poleward transport of water vapor and latent heat on climate time scales (e.g., Wu et al. 2011). It is plausible that increases in greenhouse gas concentrations could cause ARs to intensify (Dettinger 2011; Lavers et al. 2013), most directly in response to thermodynamically driven increases in atmospheric water vapor (Trenberth et al. 2003), but possibly also due to changes in midlatitude large-scale atmospheric patterns (e.g., Cohen et al. 2014; Petoukhov et al. 2013). Because ARs are so closely tied to the occurrence of extreme precipitation events in the historical record, serve as an

Corresponding author address: Daniel L. Swain, 473 Via Ortega, Stanford, CA 94305.
E-mail: dlswein@stanford.edu

important dynamical linkage between regions, and are potentially sensitive to shifts in large-scale climate, ARs are of considerable relevance for short-term weather prediction, annual-scale climate variability, and long-term climate change.

The general spatial structure and dynamic evolution of ARs over the northeastern Pacific Ocean is well characterized. Highly concentrated plumes of vertically integrated water vapor (IWV) often develop within the “warm conveyor belt” of extratropical cyclones (Sodemann and Stohl 2013), usually aligned with the pre-cold-frontal low-level jet (LLJ) band, and sometimes extending well downstream of the parent synoptic-scale system (e.g., Bao et al. 2006; Ralph et al. 2004). In situ measurements confirm that the highly anomalous IWV plumes associated with ARs are indeed spatially correlated with regions of strong water vapor transport (Ralph et al. 2004, 2005, hereafter RNR05), which has facilitated the use of IWV (directly obtainable from Earth-orbiting satellites) as a proxy for the vector quantity itself. Local evaporation and moisture convergence is thought to be the primary means by which water vapor concentrates within the distinct IWV band that characterizes ARs (Cordeira et al. 2013; Sodemann and Stohl 2013), although advective water vapor transport from low latitudes ($<23.5^{\circ}\text{N}$) may play a role in at least some AR events (Bao et al. 2006; Ralph et al. 2011).

In vertical profile, ARs over the Pacific tend to be characterized by moist-neutral stability in the lower levels (RNR05), which is a favorable condition for the orographic enhancement of precipitation (Ralph et al. 2004; RNR05). Because of the existence of south–north or southeast–northwest-oriented coastal mountain ranges along most of the Pacific coastline of North America, onshore IWV fluxes associated with strong southwesterly LLJs are often substantially orthogonal to the primary topographic axis in this region. The combination of moist-neutral stability and strong topographically forced ascent can lead to dramatic enhancement of precipitation over higher terrain (Ralph et al. 2004; RNR05; Neiman et al. 2008a), with 24-h accumulations sometimes exceeding 300–400 mm (e.g., Neiman et al. 2008b). Extreme precipitation events that occur as a result of ARs have been implicated in a large fraction of individual flood events of historical significance both along the Pacific coast and in other regions (e.g., Ralph et al. 2006; Neiman et al. 2008b; Ralph et al. 2011, 2012; Lavers et al. 2011; Neiman et al. 2011).

The finescale vertical structure of ARs is considerably more difficult to diagnose than the broadscale horizontal structure. However, this vertical structure is crucially important in determining the impact of AR events that move onshore in regions of enhanced orography (Neiman

et al. 2008a; Kingsmill et al. 2013). While broadscale AR horizontal structure can be largely understood in the context of its placement within the warm conveyor belt of synoptic-scale cyclones (Bao et al. 2006), insights into the vertical structure of ARs have come about largely within the past two decades as a result of several observational studies conducted over the Pacific Ocean (RNR05) and along the immediate Pacific coast of North America (e.g., Ralph et al. 2011; Kingsmill et al. 2013). Two of these studies, the California Land-Falling Jets Experiment (CALJET) in 1998 and the Pacific Land-Falling Jets Experiment (PACJET) in 2001, yielded an unprecedented high-resolution in situ dataset describing the vertical structure of numerous individual ARs (RNR05). During these aircraft-based field campaigns, dozens of dropsondes were deployed over the Pacific Ocean in and near the LLJ associated with well-defined ($\text{IWV} > 2 \text{ cm}$) ARs. Most of these dropsondes sampled the region along or immediately upstream of the axis of maximum IWV, resulting in a substantial number of high-quality soundings of the AR environment (RNR05). More recent field studies—especially CalWater 2015, which has garnered considerable scientific and public interest (Witze 2015)—have focused on the physical characteristics of landfalling ARs near California.

Motivated by the importance of understanding and simulating ARs on both weather and climate time scales, the present study seeks to evaluate the performance of a high-resolution atmospheric model, the Weather Research and Forecasting (WRF) Model, in representing the key features of AR vertical structure. Various numerical models are generally capable of reproducing the broadscale spatial characteristics of ARs, such as enhanced broadscale IWV plumes and IWV fluxes (Smith et al. 2010). However, relatively little is known regarding numerical model representation of the finescale variations in kinematic and thermodynamic parameters critical to the orographic enhancement that occurs during AR-associated extreme precipitation events—including the extreme values of vertically integrated moisture transport that are typically associated with ARs. The narrowness of the water vapor plumes associated with atmospheric rivers, the scarcity of in situ observations of individual plumes, and the coarseness of available water vapor observations from remote sensing platforms also complicate the evaluation of the ability of atmospheric models to simulate the finescale structure of atmospheric rivers. Given the recognized importance of these finescale details in causing intense regional precipitation events, and increasing interest in the thermodynamic and/or dynamic causes of possible changes in continental precipitation extremes, quantification of simulated biases in AR-relevant variables is a necessary step toward

understanding whether numerical models are accurately capturing the underlying mechanisms of AR-related precipitation events.

To explore these topics and close this existing gap in knowledge, we compare continuous 3-month non-hydrostatic WRF simulations with observations collected during 17 separate AR events reported in [RNR05](#). The 17 observed AR events included in this study occurred in 1998 (10 events) and 2001 (7 events). We assess various characteristics of vertical and horizontal AR structures that are captured in the WRF simulations but are not present in the atmospheric reanalysis data within which the WRF Model is nested.

2. Model and methods

To assess numerical model representation of finescale AR structure, we have completed two separate, continuous 3-month simulations using the WRF Model, version 3.2.1 ([Skamarock et al. 2005](#)). The two simulations are targeted at the dates of the CALJET and PACJET field campaigns [January–March (JFM) 1998 and JFM 2001; initialized on 1 January 1998 and 1 January 2001, respectively]. Since the earliest calendar date occurrence of any AR included in this study (in either 1998 or 2001) is 21 January, all of our analysis occurs after at least 21 days of model spinup. To achieve the very high temporal resolution necessary to sample the same region of the narrow and locally transient IWV plume as was sampled by each dropsonde, we conduct 17 separate 24-h simulations using WRF “restart” files (which obviates the need for additional spinup) at the time of each AR event, and increase the model output frequency to $1/60\text{ s}^{-1}$. Each model-derived profile, therefore, corresponds to the respective dropsonde-derived profile with a temporal error of $<60\text{ s}$.

Our WRF configuration includes a nonhydrostatic dynamical core (NMM), the WRF single-moment 5-class microphysics scheme (WSM5), the Mellor–Yamada–Nakanishi–Niino level 2.5 (MYNN 2) boundary layer scheme, and no cumulus parameterization scheme (i.e., explicit convection is allowed). Mixed-phase microphysics schemes such as WSM5 ([Hong et al. 2004](#)) better represent complex cloud processes at high spatial resolutions ([Hong and Lim 2006](#)), and have been used previously in AR simulation studies ([Leung and Qian 2009](#)). This nonhydrostatic WRF configuration is similar to that tested by [Lebassi-Habtezion and Diffenbaugh \(2013\)](#), who found that the WRF simulations using a nonhydrostatic dynamical core without cumulus parameterization produced more accurate temperature and precipitation fields across the western United States than did simulations using either a hydrostatic core or a nonhydrostatic core with

cumulus parameterizations (albeit for the summer season). We use a single large ($3600\text{ km} \times 3200\text{ km}$) domain covering much of the northeastern Pacific Ocean and the west coast of North America (19.9° – 51.2°N , 154.9° – 111.8°W) with 4-km grid spacing in the horizontal and 50 levels in the vertical. Lateral boundary conditions are provided by NCEP’s North American Regional Reanalysis (NARR) dataset ([Mesinger et al. 2006](#)), and observed sea surface temperatures (updated daily) are incorporated into the lower boundary condition using NOAA’s 0.25° satellite-derived product ([Reynolds et al. 2007](#)).

We compare the three-dimensional WRF fields with the data from the observational campaigns at the exact time and location of the published dropsonde data. Model grid boxes utilized in the construction of composite vertical profiles correspond to the latitude and longitude of actual dropsonde observations, and are centered no farther than 2.83 km from in situ sampling locations. We note that our methodology cannot eliminate the risk that model-derived profiles sample a different part of the AR environment than the original [RNR05](#) observations due to errors in WRF’s simulated spatiotemporal evolution of each individual event. Since ARs (both real world and simulated) are narrow and highly transient features, it is possible that even relatively small biases in timing of each AR could substantially affect the comparison of simulated “snapshots” with observed vertical profiles. Given the subjectivity in choosing a metric for matching the relative position of each dropsonde observation with its “most representative” location in the WRF simulations—and the lack of information in the original [RNR05](#) study regarding the specific position of each dropsonde observation in the AR environment—we opt for a maximally objective and unbiased approach in comparing observations and simulations by simply comparing the data at fixed times and locations. Our methods are aimed toward minimizing other potential errors to the greatest extent possible, primarily by ensuring high model-observation correspondence ($\sim 3\text{ km}$ in space and $\sim 60\text{ s}$ in time).

To further minimize error stemming from differing approaches in characterizing ARs, all procedures regarding the calculation of composite vertical profiles follow [RNR05](#) as closely as possible. Following [RNR05](#), we calculate the along-river water vapor flux [Flux_r , Eq. (1)] using the method described in [Ralph et al. \(2004\)](#), where z is height (m) and ρ , U , and q_{sp} are layer mean density (g m^{-3}), total wind speed (m s^{-1}), and mixing ratio (g kg^{-1}), respectively:

$$\text{Flux}_r = W_r \int_{Z_{1000}}^{Z_{500}} \rho U q_{\text{sp}} \partial Z. \quad (1)$$

We define W_r as the mean atmospheric river width (viz., the width of the most concentrated part of the IWV plume and the corridor of maximum water vapor flux). The quantity W_r is estimated to be 100 km in RNR05 (a 50-km margin around each dropsonde observation), so we make the same approximation here for consistency [though we note that Ralph et al. (2004) find that actual atmospheric river width is closer to 400 km]. The quantity Z is subdivided into 10 equal 50-mb (1 mb = 1 hPa) increments from 975 to 525 mb (layer means between 1000 and 500 mb). Note that Flux_r can also be defined as the product of W_r and the (vertically) integrated vapor transport (IVT).

The calculation of vertical profiles for all variables other than Flux_r is accomplished by interpolating quantities onto a 100-m resolution vertical grid, which is the same grid used in RNR05. After WRF-simulated data corresponding to each of the 17 observed soundings are interpolated, three separate composite model vertical profiles are constructed: the total composite, which includes data from 15 AR events (and excludes data from a single event on two successive sampling dates; see section 3a); the 1998 composite, which includes data from 11 AR events occurring during 1998; and the 2001 composite, which includes data from 4 AR events occurring during 2001. These individual and composite profiles are used to compare WRF Model output directly to the in situ observations reported in RNR05.

We also emphasize the additional caveat that the 17 ARs examined in RNR05 (and thus in the present study) constitute neither a complete nor necessarily a representative sample of all AR events occurring in 1998 and 2001. The primary aim of our analysis is an objective comparison of WRF Model simulations and the observational data published in RNR05. To facilitate this comparison, we show composite profiles for each year separately so that they may be directly compared to the RNR05 profiles (despite the small sample size and potential lack of robust, statistically significant differences between composites).

3. WRF simulation results and comparison to observations and reanalysis

a. AR horizontal spatial characteristics

We begin our analysis by noting the existence of well-defined and narrow simulated IWV plumes in 15 of the 17 cases considered in this study (Fig. 1). The core of the simulated IWV plume is located near the geographic location of dropsonde measurements in 15 out of 17 cases. (The two exceptions, which are generally unrepresentative of the AR environment, are discussed at the end of this subsection.) This spatial correspondence suggests that WRF generally captures the propagation and evolution of the ARs across a large nested domain.

The enhanced IWV plumes in each study case are also spatially coincident with large vertically integrated water vapor fluxes, which at times exceed 500 kg m s^{-1} near the AR axis (results discussed in section 3c). Water vapor fluxes are strongest in the lower troposphere around 925 hPa, where low-level winds are strong and mixing ratio tends to be high (Figs. 2d,f). A total of 15 out of 17 IWV plumes in this study exhibit considerable meridional extent (Fig. 1), and low-level winds in the vicinity of each AR are largely parallel to each IWV axis. The WRF-simulated local mean ratio of meridional IVT to zonal IVT within the AR plumes [i.e., the arithmetic mean of 15 individual ratios ($\text{IVT}_{\text{meridional}}/\text{IVT}_{\text{zonal}}$) calculated separately for each modeled AR event, excluding the two events discussed earlier] is 4.9. However, zonal IVT exceeds meridional IVT in 6 out of 15 events, and the overall meridional–zonal mean ratio for the 15-member composite is only 1.04—suggesting that those ARs with a high $\text{IVT}_m/\text{IVT}_z$ ratio were relatively weak, and that net zonal and meridional contributions to IVT are comparable when averaged over all events.

The most notable difference between the WRF-simulated IWV plumes and those sampled by dropsondes in RNR05 occurs for the 12 February and 13 February 2001 observations (Figs. 1m,n), which comprise two successive samplings of the same distinct AR event. In these two cases, the model-derived vertical profiles are notably different from the observations in RNR05, exhibiting lower potential temperature, lower mixing ratio, and lighter winds (not shown) than simulated by WRF during the other 15 events or observed in RNR05 during all 17 events (Figs. 2 and 3). Model output fields and GOES-10 infrared satellite imagery (not shown) both depict a slow-moving cyclonic circulation centered approximately 800 km off of the California coast during this event. Based on examination of reanalysis 250–500-mb wind fields and interpretation of satellite imagery (not shown), this circulation appears to be largely cut off from the mean zonal flow, with no AR signature apparent prior to 12 February 2001. We also note that the WRF simulations of the 12–13 February 2001 event depict a poorly defined AR relative to others in the study (Figs. 1m,n). The large differences between the observed and simulated AR profiles for the 12–13 February 2001 event appear to be caused by errors in the WRF-simulated location of the parent cyclone, resulting in the absence of AR conditions at the spatiotemporal point of interest. Because our primary focus is on simulated finescale AR structure, the absence of a distinct AR in WRF simulations of this event leads us to exclude data from 12 February 2001 and 13 February 2001 in both the overall and 2001 composites. Real-world (and simulated) cutoff lows are known to exhibit erratic trajectories

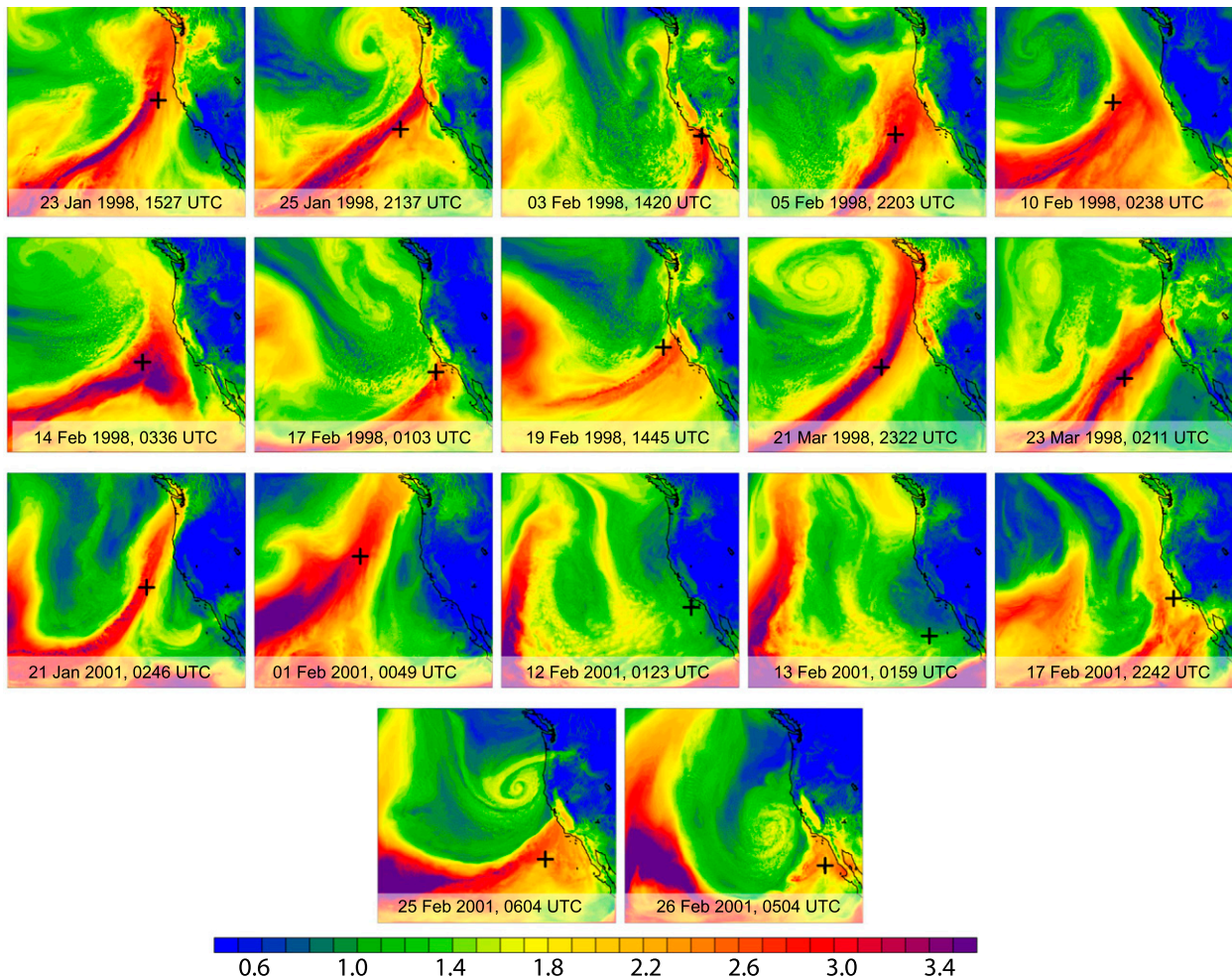


FIG. 1. Snapshots of WRF IWV (cm) from (top left) 23 Jan 1998 to (bottom right) 26 Feb 2001. Black plus signs denote the location of [RNR05](#) dropsonde observations at the time of each snapshot.

([Nieto et al. 2005](#)), and a comprehensive investigation into the source of WRF errors for this particular system is beyond the scope of the present study. We do acknowledge, however, that this case represents a substantial failure of WRF to accurately simulate the large-scale conditions relevant to the initiation and propagation of an observed AR, and we therefore suggest that this issue could be a focus of future work.

b. Vertical structure of water vapor transport and thermodynamic variables in ARs

[RNR05](#) and others highlight several defining characteristics of the AR environment: the presence of a well-defined, narrow plume of concentrated IWV; collocation of a LLJ with the maximum horizontal water vapor flux centered ~ 1 km MSL; moist neutral stability in the lower troposphere; and nearly saturated conditions below ~ 2 km MSL. The last three of these conditions play important roles in the strong orographic enhancement

of precipitation associated with AR events, and thus we focus on these quantities for much of the remaining analysis.

The simulated composite profile for the 1998 and 2001 events depicts a local maximum in wind speed of $\sim 19 \text{ m s}^{-1}$ near 0.8 km MSL (940 hPa, [Fig. 2d](#)). This composite feature is somewhat weaker and slightly lower in altitude than the $\sim 23 \text{ m s}^{-1}$ LLJ centered at ~ 1 km reported in [RNR05](#). However, there is a distinct difference between the composites for 1998 and 2001: the 1998 composite depicts a mean LLJ strength of $\sim 23 \text{ m s}^{-1}$ and an altitude of ~ 0.9 km (920 hPa), while the 2001 composite has a much weaker ($\sim 13.5 \text{ m s}^{-1}$) and lower (~ 0.6 km, 950 hPa) LLJ signature. In all three composite profiles, the mixing ratio decreases monotonically with height [with the minor exception of a thin layer of little change around 1 km (900 mb) in the 2001 composite], with a near-surface value of $\sim 9 \text{ g kg}^{-1}$ in both the simulated and observed composites. At all heights, the mixing

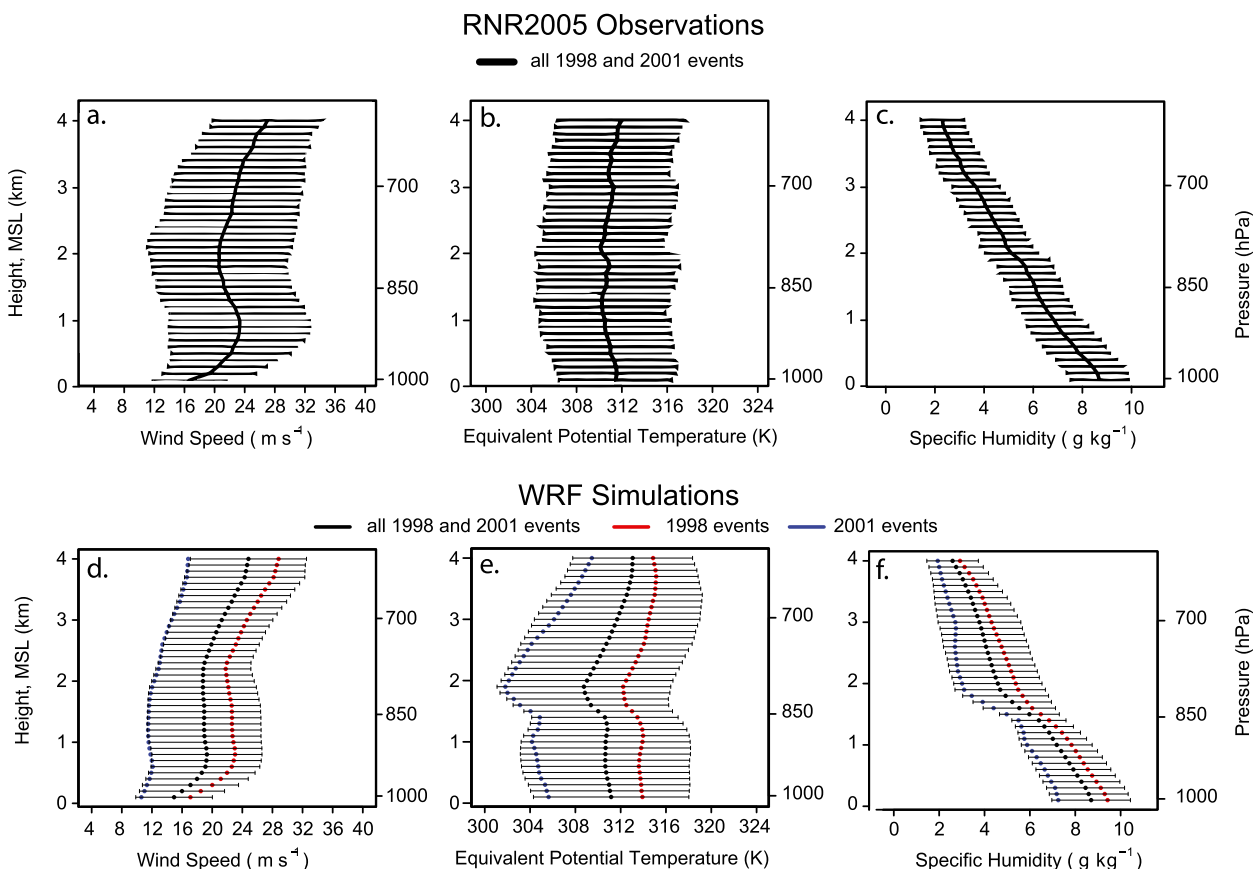


FIG. 2. Composite vertical profiles of the AR environment—(left to right) wind speed, θ_e , and q_{sp} —adapted from (a)–(c) **RNR05** and (d)–(f) derived from WRF output. Black curves in (a)–(c) and points in (d)–(f) denote overall (1998 + 2001) composites. Red (blue) points in (d)–(f) denote 1998 (2001) composites. The horizontal black bars represent \pm one standard deviation of each variable at each vertical level.

ratio is higher in 1998 than in 2001 by as much as 2 g kg^{-1} (Fig. 2f). All three composites exhibit a region of sharp drying with height between 850 and 800 hPa, particularly in the 2001 composite. This dry region—which is not apparent in **RNR05**—has implications for the interpretation of thermodynamic quantities (discussed later in this section).

Simulated along-river water vapor flux (defined as the instantaneous advective transport in the direction of the local total wind vector) exhibits a distinct maximum around 0.8 km MSL (925 hPa), which is close to the reported **RNR05** value (Figs. 3e,f). This peak in along-river water vapor flux is collocated with the simulated LLJ in both the overall composite and the 1998 composite (Fig. 2d), with fluxes decreasing with height above 900 hPa. The vertical structure of water vapor flux in WRF is largely consistent with the **RNR05** findings, though the wind speed maximum associated with the LLJ in the overall WRF composite is less distinct than in either the **RNR05** composite (Figs. 2a,d) or individual simulated events (not shown). In contrast, the water vapor flux composite profile for 2001 does not exhibit a

distinct low-level flux maximum, and is much weaker overall. Indeed, the maximum flux in the 1998 composite is nearly double that of the 2001 composite ($\sim 100 \times 10^5 \text{ kg s}^{-1}$ in 1998 vs $\sim 50 \times 10^5 \text{ kg s}^{-1}$ in 2001). Given the importance of the LLJ in driving strong water vapor fluxes in ARs, this contrast in water vapor flux between the 1998 and 2001 composites can largely be explained by the lack of a clear LLJ maximum in the simulated 2001 wind composite (Fig. 2d). **RNR05** find a similar difference between total along-river flux profiles for 1998 and 2001 (not shown).

Vertical profiles of thermodynamic parameters are also calculated. Potential temperature profiles depict an atmosphere absolutely stable to dry convection at all levels ($d\theta/dz > 0$ everywhere) (not shown). Consistent with observations, 1998 exhibits higher values than 2001 throughout the column. However, given the role of conditional parcel saturation by orographic forcing and moist-neutral stability in the generation of heavy, orographically enhanced precipitation, equivalent potential temperature (θ_e , shown in Fig. 2e) is a more relevant metric of stability in an AR environment (e.g., **Ralph et al. 2004**). All

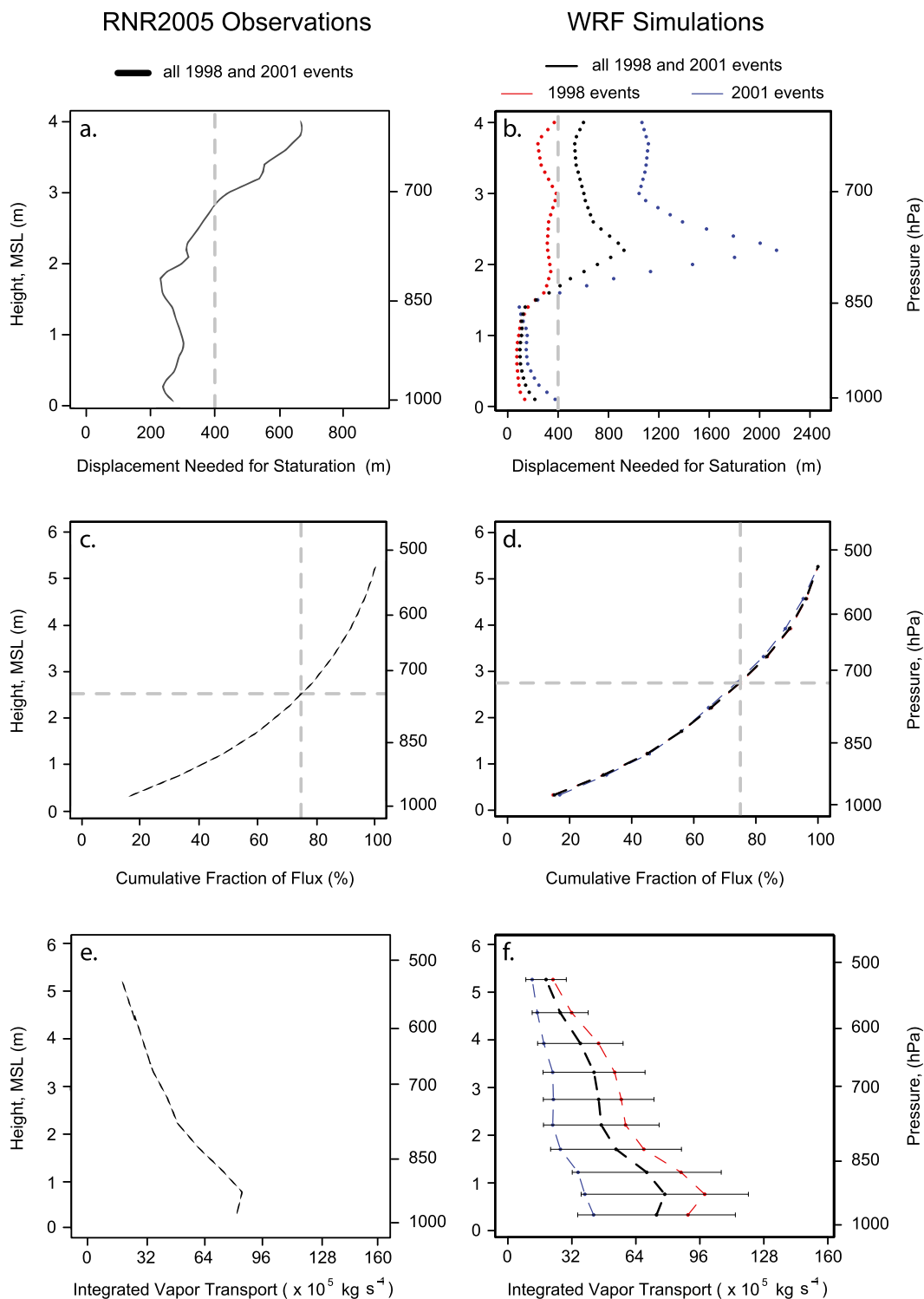


FIG. 3. Composite vertical profiles of the AR environment—(a),(b) displacement needed for saturation, (c),(d) cumulative fraction of flux, and (e),(f) integrated vapor transport—adapted from (left) **RNR05** and (right) derived from WRF output. The curves (solid or dashed) and points in b, d, and f—black, red, and blue—denote overall (1998 + 2001), 1998, and 2001 composites, respectively. The horizontal black bars in (f) represent \pm one standard deviation of integrated vapor transport at each vertical level.

three simulated θ_e profiles exhibit a relatively deep region of moist neutral conditions ($d\theta_e/dz \sim 0$) between the surface and ~ 850 hPa (Fig. 2e), in agreement with the observed composite profiles (Fig. 2b). However, the simulated profiles also contain a distinct conditionally unstable ($d\theta_e/dz < 0$) layer between 850 and 800 hPa that is much less pronounced in the observational composites. This layer corresponds to the region of sharp drying observed in the mixing ratio composites (Fig. 2f). Though there is some suggestion that conditionally unstable conditions in the lower troposphere do occur in at least some AR events (Neiman et al. 2008b; Kingsmill et al. 2013), this elevated layer of conditional instability in the model composites appears to be a direct result of the low mixing ratio simulated at the corresponding height level (Fig. 2f). We also note that (except for the thin region of conditional instability discussed above), approximate moist neutrality ($d\theta_e/dz \sim 0$) extends from near the surface to around 2.1 km (Fig. 2e), which is considerably below the RNR05 reported height of ~ 3.0 km (Fig. 2b). However, $d\theta_e/dz$ in the WRF composites remains small ($< 2 \text{ K km}^{-1}$) between 2.1 and 4 km.

As mentioned above, the extreme precipitation often associated with landfalling ARs along the Pacific coast is primarily caused by strong orographic lift acting on a nearly saturated air mass with moist-neutral stability (Ralph et al. 2004, 2006). To assess the potential for the air in the AR environment to become saturated by orographic forcing, we calculate the vertical distance that each 100-m layer would have to be lifted to reach the lifting condensation level (LCL). Following the methodology of RNR05, we assume that all parcels requiring less than 400 m of lift to reach saturation will do so after moving onshore (with 400 m being the minimum height of California's coastal mountains presumed by RNR05). In accordance with observations, simulated requisite displacements are less than 400 m for a rather deep layer of the troposphere from the surface up to at least 850 hPa (Fig. 3b). In the simulated 1998 profile, the requisite displacement is less than 400 m through the entire column up to ~ 620 hPa. In contrast, the RNR05 composites show that the parcels above ~ 850 hPa consistently require more than 400 m displacement for saturation (Fig. 3a). The large displacement (> 500 m) required for saturation around ~ 800 hPa in the 2001 profile appears to be a direct result of the dry atmospheric region discussed above.

RNR05 note that the humidity sensors used to sample the AR environments exhibit a significant, relative humidity-dependent dry bias on the order of $\sim 10\%$. Correction of this observational bias was not possible in the RNR05 study. Thus, this observational error is

propagated into the observational composite humidity profiles, and subsequently into observational profiles of other humidity-dependent variables (RNR05). Because relative humidity is presumed to be essentially constant (i.e., near 100%) in the lower troposphere following topographically forced ascent, RNR05 point out that this dry bias should not qualitatively affect interpretation of stability parameters in the already-saturated zone (as $d\theta_e/dz$ remains near zero regardless), although it will substantially decrease the calculated vertical displacements required for saturation. Our model results suggest that the vertical displacements required for saturation are indeed less than reported by RNR05—not only in the low levels below ~ 850 hPa, but through nearly the entire atmospheric column up to around 650 hPa. However, a comprehensive characterization of this error is not possible based on the data available, since details degrading the RH sensor error profile at different vertical levels remain unknown. Thus, we mention this possible source of error simply to highlight the fact that observational uncertainty in the original RNR05 study has the potential contribute a nonnegligible portion of the difference between simulated and observed moisture variables (especially at lower atmospheric levels).

c. Assessment of model simulation of key variables

Three variables are chosen to quantitatively assess overall model performance for each AR event: IWV, the magnitude of the total wind at 1 km MSL, and the vertically integrated along-river water vapor flux. Simulated values for each of these quantities are compared to observed values from RNR05. We find that WRF overestimates IWV [WRF values $+5.9\%$ (~ 0.15 cm) greater than RNR05 values] for most events (Fig. 4a), although this bias is generally small, and relatively uniform across AR events. Simulated 1-km MSL winds, on the other hand, exhibit larger negative biases (-17.7%) with respect to observations (Fig. 4b), particularly for the stronger AR events. For example, the strength of the WRF-simulated winds is approximately half of the observed values for the strongest observed event ($\sim 20 \text{ m s}^{-1}$ simulated, $\sim 40 \text{ m s}^{-1}$ observed). However, WRF does capture the pattern of much stronger 1-km winds in 1998 than in 2001. Finally, RNR05 report that 75% of cumulative AR water vapor transport occurred below ~ 2.50 km—a product of sharply decreasing humidity with height and a LLJ maximum near ~ 1 km. WRF composites depict a similarly sharp attenuation with height, albeit with a slightly higher altitude (2.75 km) for the 75% benchmark (Figs. 3c,d).

WRF also underestimates the vertically integrated along-river water vapor flux for the strongest observed AR events (Fig. 4c), although the relative magnitude of

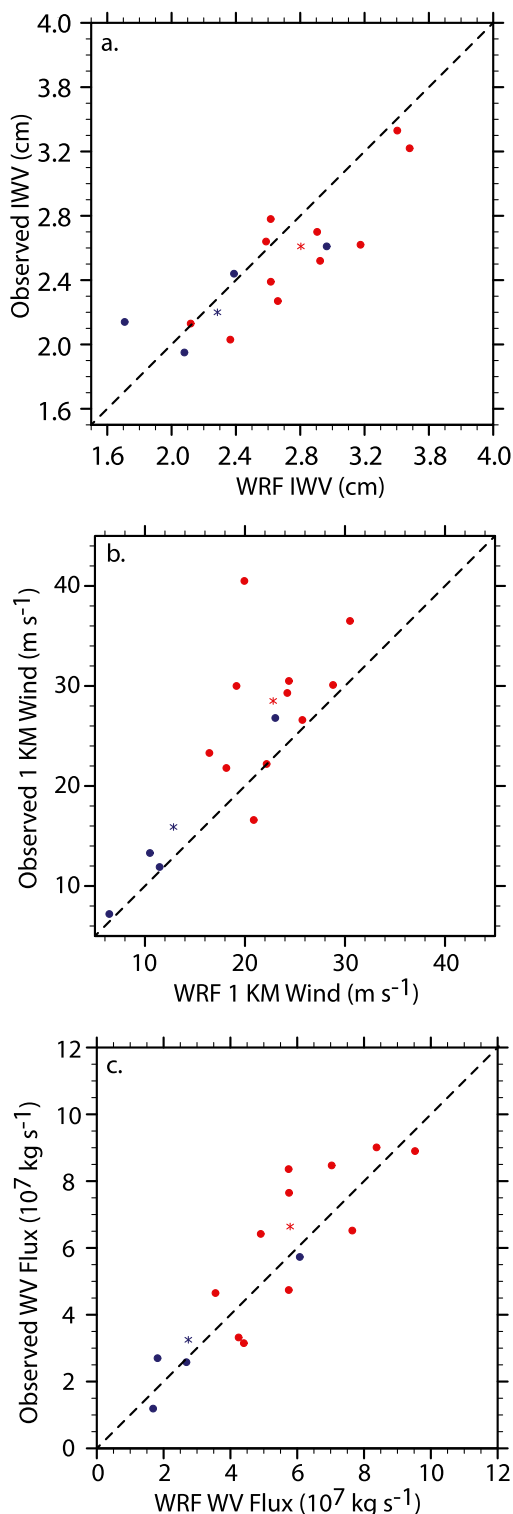


FIG. 4. Scatterplot showing observed vs model values for (a)–(c) IWV, 1-km wind speed, and vertically integrated water vapor flux. Red (blue) circles represent observation–model pairs for 1998 (2001), and black lines are 1:1 lines. Red (blue) asterisks denote the composite mean values for 1998 (2001).

this bias (-11.2% overall) is not as large as for 1-km winds. Because along-river water vapor transport essentially aggregates the overall effects of winds and water vapor at all levels, there may be an element of compensating bias in this metric due to the slight overestimate of integrated water vapor and the stronger underestimate of 1-km winds. However, interpretation of the vertical wind profiles for each separate event (not shown) indicates that the altitude of the LLJ simulated in WRF is more variable and on average lower in the atmosphere ($\sim 1.0 \text{ km}$ in RNR05 vs $\sim 0.8 \text{ km}$ in WRF). This bias results in vertical “smoothing” of the overall composite wind profile and lower composite maximum LLJ wind velocity ($\sim 20 \text{ m s}^{-1}$ in WRF composite), despite the presence of comparable maxima for both individual WRF events and the RNR05 composite ($\sim 23 \text{ m s}^{-1}$ in both). Given this smoothing effect, total model-simulated vertically integrated fluxes would indeed be expected to have greater correspondence with observations than the winds at a particular altitude (i.e., 1 km). Since ARs are highly transient and anomalously intense atmospheric features at any particular location, the fact that model-simulated values at specific spatiotemporal points are close to the observed values suggests that the nonhydrostatic WRF configuration captures not only the evolution and propagation of ARs across a large domain, but also the extreme IVT values associated with each AR.

The localized nature of dropsonde sampling in RNR05 does not allow for direct comparison between two-dimensional horizontal patterns of IVT from WRF simulations and those from in situ observations. However, it is possible to compare the two-dimensional vertical instantaneous point observations to analogous profiles extracted from the two-dimensional horizontal IVT field in WRF and NARR. We report results obtained by calculating the IVT field at each dataset’s native resolution (4 km for WRF and $\sim 32 \text{ km}$ for NARR) and regriding (using a bilinear interpolation scheme) to a common 0.30° ($\sim 32 \text{ km}$) grid. We test the sensitivity of our results to the coarseness of the regriding scheme used [including 0.04° ($\sim 4 \text{ km}$) and 0.30° ($\sim 32 \text{ km}$) resolutions], and find that our results are robust across this wide range of resolutions (not shown). We find that the local instantaneous IVT simulated by WRF at these locations is greater than that in NARR in all instances, with WRF values generally $>100\%$ higher than NARR values (not shown). Observed IVT values from RNR05 are very similarly distributed, with 80% of values falling above those from NARR, and $>50\%$ exceeding NARR by more than 100% (not shown). Overall, we find that—relative to NARR—local IVT in the vicinity of each WRF-simulated AR is much closer to that found in the in situ observations (see frequency distributions in Fig. 5).

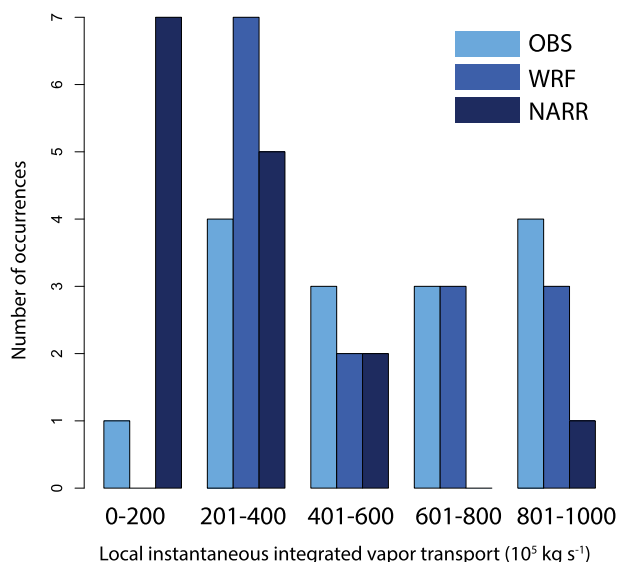


FIG. 5. Histogram depicting number of occurrences (0–7) of local instantaneous IVT per 100 km of AR width. Dark blue denotes NARR values, lighter blue WRF values, and lightest blue RNR05 observations.

Figure 6 depicts domain-wide instantaneous IVT from the WRF and from the NARR reanalysis, both interpolated to a common ~ 32 -km grid. Because the relevant NARR fields are available only at 3-hourly intervals, there is up to a 3-h difference between the time of WRF and NARR snapshots, meaning that in several instances there is a noticeable spatiotemporal mismatch between ARs depicted in WRF and NARR, which prevents simple differencing of the 2D fields. However, comparison of the AR representation in WRF and NARR is still possible through visual assessment of the IVT fields. The narrow corridors of strong IVT associated with the ARs are clearly visible in most of the WRF simulations, but are generally much less distinct in NARR. The AR-associated maxima in these horizontal IVT fields are notably larger in the WRF data relative to the NARR data, which is consistent with our earlier results derived from instantaneous vertical profiles for the same events (Figs. 3e,f). While systematic sensitivity analysis of the role of horizontal and vertical model resolution is beyond the scope of this study, these findings suggest that the high-resolution WRF simulations capture finescale physical processes that are not captured in the atmospheric model underlying NARR, and that this enhanced “information” (viz., finescale AR structure and extreme IVT maxima) is partially retained even when WRF fields are interpolated to a coarser grid. Combined with the agreement between the simulated point IVT values and in situ observations, these results demonstrate that the nonhydrostatic WRF configuration is capable of accurately simulating the

extreme water vapor fluxes associated with ARs, even when these extreme values are not present at the scale of the boundary conditions provided to the model.

As is extensively discussed in RNR05, the 1998 CALJET field campaign took place during one of the most pronounced El Niño events of the twentieth century [January multivariate ENSO index (MEI, calculated bimonthly) value = 2.48], and the 2001 PACJET campaign during a weak La Niña event (January MEI = -0.54 ; data obtained from ESRL 2015). Thus, it is plausible that large-scale conditions over the eastern Pacific basin—and thus the character of ARs in these years—were influenced by opposing ENSO states (RNR05). Indeed, simulated AR events in 1998 are generally warmer, wetter, and more intense than those occurring in 2001 (Figs. 2 and 3), which is consistent with findings in RNR05 (not shown). The AR-localized point IVT values (i.e., at locations corresponding to dropsonde sampling in RNR05) are 66% higher in the 1998 WRF composite, and 56% higher in the 1998 NARR composite. Of the 15 AR events sampled, the 5 most intense all occur in 1998.

WRF-simulated full-domain composites (including all 17 dates) of 500-hPa geopotential heights depict a distinctly different synoptic-scale flow for AR events in 1998 and 2001. In 1998, a deep trough is present in the Gulf of Alaska (Fig. 7a), directing a long zonal fetch of Pacific air into California. A trough is present just west of California and Oregon in 2001, with a less zonally oriented pattern over the east Pacific (Fig. 7b). Comparison of these composites to NARR reanalysis fields and to analogous composites presented in RNR05 suggests that WRF accurately captures these broadscale differences, though the simulations exhibit substantially stronger ridging along the Pacific coast in 1998 than occurs in reanalysis (Fig. 7c), along with deeper troughing west of California in 2001 (Fig. 7d). The latter discrepancy appears to be driven mostly by the 12–13 February 2001 event in which WRF poorly simulates the anomalous cutoff circulation near the California coast (discussed in section 3a).

We note that the WRF domain used in this study is much larger than is typically used in nested, ultra-high-resolution nonhydrostatic simulations ($3600 \text{ km} \times 3200 \text{ km}$ at 4-km resolution), and is apparently large enough to allow for noticeable synoptic-scale differences to develop over the course of long-running (3 month) integrations (relative to the NARR reanalysis within which WRF is nested). A comprehensive diagnosis of the causes of these large-scale departures between the nested WRF simulations and the NARR reanalysis is beyond the scope of this study, although we note that despite these differences WRF simulations generally reproduce the individual ARs in the proper spatiotemporal context, and with realistic intensity. We further emphasize that it is not possible using the

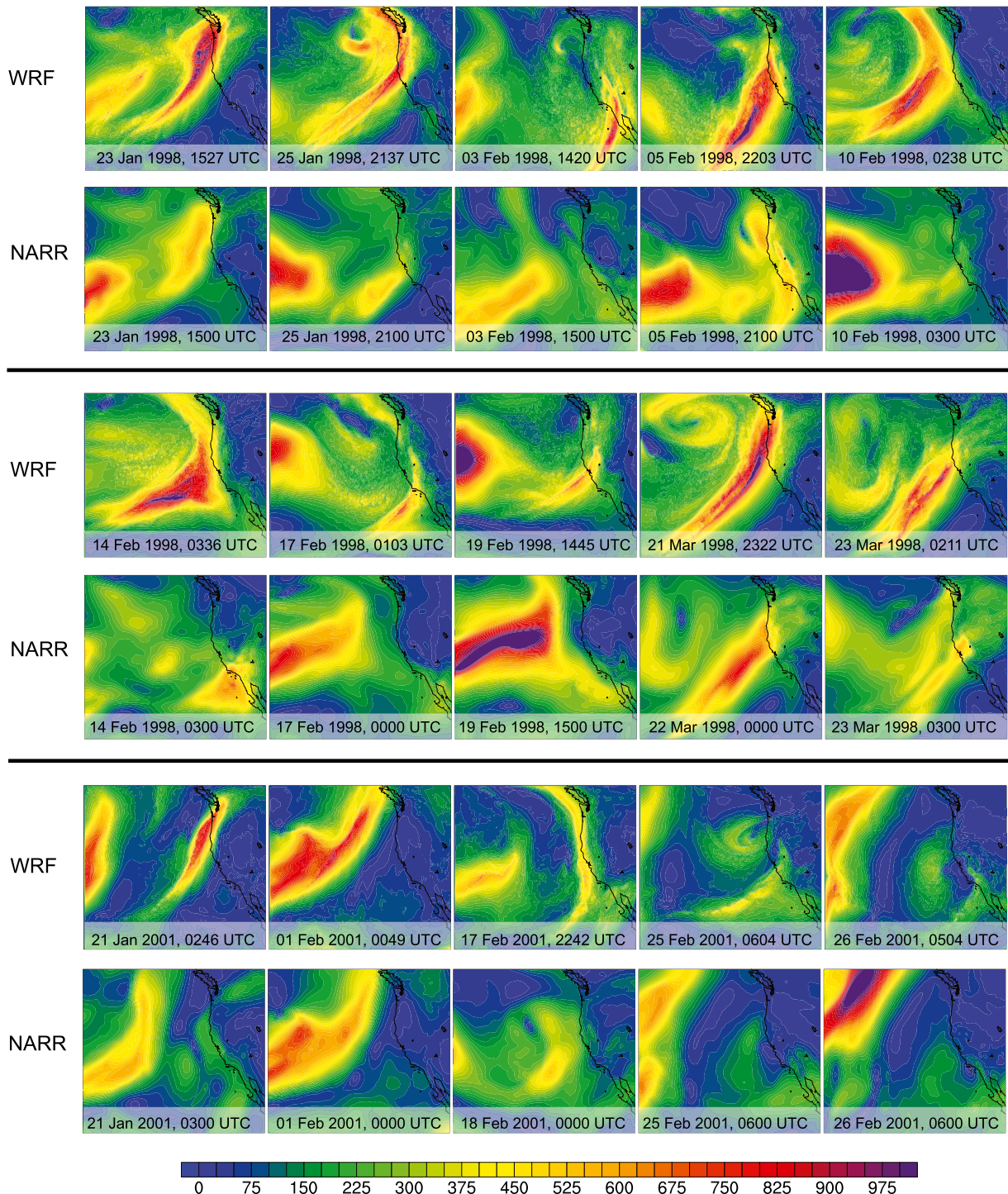


FIG. 6. Snapshots of IVT ($\text{kg m}^{-1} \text{s}^{-1}$) for (first, third, and fifth rows) WRF simulations and (second, fourth, and sixth rows) NARR data for (top) 23 Jan to 10 Feb 1998, (middle) 14 Feb to 23 Mar 1998, and (bottom) 21 Jan to 26 Feb 2001. All data are interpolated to a common ~ 32 -km grid. Note the <3 -h differences in timestamps between WRF and NARR snapshots for corresponding events.

present methodology to attribute the simulated differences between AR events in 1998 and 2001 to any specific large-scale forcing mechanism, including ENSO. As noted earlier, the AR events in this study do not

comprise a representative sample of all AR events in each year (a product of experimental constraints in the original [RNR05](#) work), and the overall number of AR events included in this study is too small to draw

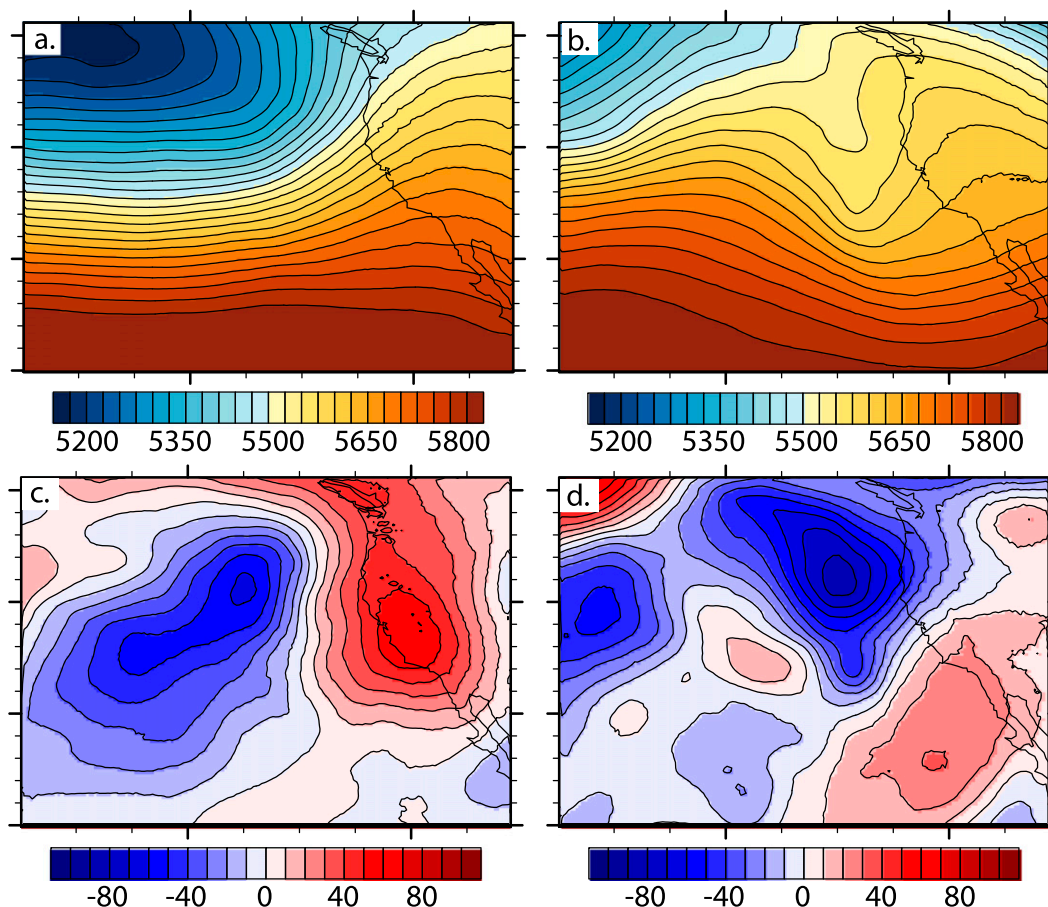


FIG. 7. Composite WRF 500-hPa geopotential height fields (contours and colored shading, m) over the full WRF domain for (a) 1998 and (b) 2001 at “snapshot” times corresponding to [RNR05](#) dropsonde observations. Corresponding differences (WRF – NARR) from reanalysis in (c) 1998 and (d) 2001.

statistically significant conclusions regarding the differences between years. We therefore include this discussion of the differences between years primarily to serve as an additional point of comparison between the present work and the original [RNR05](#) observational findings.

4. Conclusions

We compare model-simulated vertical profiles for AR environments that occurred over the northeastern Pacific Ocean during 1998 and 2001 with corresponding profiles derived from in situ dropsonde observations taken during the CALJET and PACJET field campaigns (and reported in [RNR05](#)). We find that the vertical structures of WRF-simulated AR environments are generally similar to the observed vertical structures. In addition, key features characteristic of observed AR events are generally well represented in the WRF simulations, including 1) the presence of a LLJ collocated with the vertical maximum in along-river water vapor flux, 2) the

development of a narrow and highly concentrated IWV/IVT plume, and 3) the existence of nearly saturated conditions in the lower troposphere. The magnitudes of simulated IVT, an aggregate metric of AR intensity, are close to those observed for both the overall mean and for individual events (despite biases in constituent variables).

We find simulated and observed static stability and orographic displacement parameters to be generally in agreement, with the notable exception of a layer of decreased stability and increased requisite displacements centered near 850 hPa in the WRF composites. Consistent with [RNR05](#) and others (e.g., [Neiman et al. 2008a](#); [Kingsmill et al. 2013](#)), we find that approximately moist-neutral stability and small requisite displacements occur through most of the lower troposphere during AR events. However, our simulations also depict a layer of conditionally unstable conditions centered on 850 hPa. This possibly erroneous layer of decreased stability appears to be caused by a vertical region of low mixing ratio in WRF. Additionally, we suggest that the previously reported dry

bias in the original in situ instrumentation could account for some of the difference between simulated and observed requisite displacement at higher levels (above 850 hPa). Given the importance of moist neutrality in the generation of orographically enhanced precipitation during AR events, it is plausible that such a discrepancy could influence the simulation of precipitation when AR events move onshore and interact with coastal terrain. For this reason, further study of both model-simulated thermodynamic structure of ARs over the open ocean and the subsequent precipitation on land would be highly useful in diagnosing the source of this possible model bias, and thereby in improving precipitation forecasts.

Accurate representation of AR structure in numerical models is crucial both in the context of operational meteorology and for broader investigation of the climate system. Real-time AR forecasts can provide valuable lead time for extreme precipitation events (and subsequent flooding) across much of coastal western North America (Dettinger et al. 2011; Neiman et al. 2008a). In addition, interannual variability of precipitation can be strongly influenced by the number and intensity of ARs (Dettinger et al. 2011; Dettinger 2013). Further, since intense precipitation events in a number of regions globally are intrinsically tied to the strong IVTs associated with ARs, quantifying the response of midlatitude precipitation extremes to elevated greenhouse forcing will require understanding of how the frequency and/or intensity of ARs change in response (Dettinger 2011; Lavers et al. 2013).

While it is reasonable to expect that high-resolution simulations would have a greater potential to provide a more accurate representation of finescale AR structure than low-resolution simulations, this supposition has heretofore not been demonstrated in the published literature. We find that a high-resolution, nonhydrostatic WRF configuration is capable of simulating AR structures—including localized IVT extrema—that are not present in coarse boundary conditions (even when both are interpolated to the same coarse grid), indicating that the model successfully generates finescale AR properties that are not present at the scale of the intermediate-resolution boundary conditions. These findings suggest that nonhydrostatic model configurations can offer important insights about AR structure and dynamics, particularly in instances where accurate knowledge of water vapor flux maxima is required, such as short-term weather forecasting or the analysis of extreme hydrometeorological events in a broader climate context.

Acknowledgments. We thank the National Centers for Environmental Prediction (NCEP) for providing access to the North American Regional Reanalysis (NARR).

The WRF simulations were conducted at the Center for Computational Earth and Environmental Science (CEES) at Stanford University. We acknowledge support from NSF Award 0955283, NIH Award 1R01AI090159-01, and DOE Award DE-SC00517.

REFERENCES

- Bao, J., S. Michelson, P. J. Neiman, F. M. Ralph, and J. M. Wilczak, 2006: Interpretation of enhanced integrated water vapor bands associated with extratropical cyclones: Their formation and connection to tropical moisture. *Mon. Wea. Rev.*, **134**, 1063–1081, doi:10.1175/MWR3123.1.
- Cohen, J., and Coauthors, 2014: Recent Arctic amplification and extreme mid-latitude weather. *Nat. Geosci.*, **7**, 627–637, doi:10.1038/ngeo2234.
- Cordeira, J. M., F. M. Ralph, and B. J. Moore, 2013: The development and evolution of two atmospheric rivers in proximity to western North Pacific tropical cyclones in October 2010. *Mon. Wea. Rev.*, **141**, 4234–4255, doi:10.1175/MWR-D-13-00019.1.
- Dettinger, M. D., 2011: Climate change, atmospheric rivers, and floods in California—A multimodel analysis of storm frequency and magnitude. *J. Amer. Water Resour. Assoc.*, **47**, 514–523, doi:10.1111/j.1752-1688.2011.00546.x.
- , 2013: Atmospheric rivers as drought busters on the U.S. west coast. *J. Hydrometeor.*, **14**, 1721–1732, doi:10.1175/JHM-D-13-02.1.
- , F. M. Ralph, T. Das, P. J. Neiman, and D. R. Cayan, 2011: Atmospheric rivers, floods and the water resources of California. *Water*, **3**, 445–478, doi:10.3390/w3020445.
- ESRL, 2015: Teleconnection index page. Accessed 30 December 2014. [Available online at <http://www.esrl.noaa.gov/psd/data/correlation/mei.data>.]
- Hong, S., and J. Lim, 2006: The WRF Single-Moment 6-Class Microphysics Scheme. *J. Korean Meteor. Soc.*, **42**, 129–151.
- , J. Dudhia, and S. Chen, 2004: A revised approach to ice microphysical processes for the bulk parameterization of clouds and precipitation. *Mon. Wea. Rev.*, **132**, 103–120, doi:10.1175/1520-0493(2004)132<0103:ARATIM>2.0.CO;2.
- Kingsmill, D. E., P. J. Neiman, B. J. Moore, M. Hughes, S. E. Yuter, and F. M. Ralph, 2013: Kinematic and thermodynamic structures of Sierra barrier jets and overrunning atmospheric rivers during a landfalling winter storm in northern California. *Mon. Wea. Rev.*, **141**, 2015–2036, doi:10.1175/MWR-D-12-00277.1.
- Lavers, D. A., R. P. Allan, E. F. Wood, G. Villarini, D. J. Brayshaw, and A. J. Wade, 2011: Winter floods in Britain are connected to atmospheric rivers. *Geophys. Res. Lett.*, **38**, L23803, doi:10.1029/2011GL049783.
- , —, G. Villarini, B. Lloyd-Hughes, D. J. Brayshaw, and A. J. Wade, 2013: Future changes in atmospheric rivers and their implications for winter flooding in Britain. *Environ. Res. Lett.*, **8**, 034010, doi:10.1088/1748-9326/8/3/034010.
- Lebassi-Habtezion, B., and N. S. Diffenbaugh, 2013: Non-hydrostatic nested climate modeling: A case study of the 2010 summer season over the western United States. *J. Geophys. Res. Atmos.*, **118**, 10 944–10 962, doi:10.1002/jgrd.50773.
- Leung, L. R., and Y. Qian, 2009: Atmospheric rivers induced heavy precipitation and flooding in the western U.S. simulated by the WRF regional climate model. *Geophys. Res. Lett.*, **36**, L03820, doi:10.1029/2008GL036445.
- Mesinger, F., and Coauthors, 2006: North American Regional Reanalysis. *Bull. Amer. Meteor. Soc.*, **87**, 343–360, doi:10.1175/BAMS-87-3-343.

- Neff, W., G. P. Compo, F. M. Ralph, and M. D. Shupe, 2014: Continental heat anomalies and the extreme melting of the Greenland ice surface in 2012 and 1889. *J. Geophys. Res. Atmos.*, **119**, 6520–6536, doi:[10.1002/2014JD021470](https://doi.org/10.1002/2014JD021470).
- Neiman, P. J., F. M. Ralph, G. A. Wick, J. D. Lundquist, and M. D. Dettinger, 2008a: Meteorological characteristics and overland precipitation impacts of atmospheric rivers affecting the west coast of North America based on eight years of SSM/I satellite observations. *J. Hydrometeorol.*, **9**, 22–47, doi:[10.1175/2007JHM855.1](https://doi.org/10.1175/2007JHM855.1).
- , —, —, Y. Kuo, T. Wee, Z. Ma, G. H. Taylor, and M. D. Dettinger, 2008b: Diagnosis of an intense atmospheric river impacting the Pacific Northwest: Storm summary and offshore vertical structure observed with COSMIC satellite retrievals. *Mon. Wea. Rev.*, **136**, 4398–4421, doi:[10.1175/2008MWR2550.1](https://doi.org/10.1175/2008MWR2550.1).
- , L. J. Schick, F. M. Ralph, M. Hughes, and G. A. Wick, 2011: Flooding in western Washington: The connection to atmospheric rivers. *J. Hydrometeorol.*, **12**, 1337–1358, doi:[10.1175/2011JHM1358.1](https://doi.org/10.1175/2011JHM1358.1).
- Nieto, R., and Coauthors, 2005: Climatological features of cutoff low systems in the Northern Hemisphere. *J. Climate*, **18**, 3085–3103, doi:[10.1175/JCLI3386.1](https://doi.org/10.1175/JCLI3386.1).
- Oort, A., 1971: The observed annual cycle in the meridional transport of atmospheric energy. *J. Atmos. Sci.*, **28**, 325–339, doi:[10.1175/1520-0469\(1971\)028<0325:TOACIT>2.0.CO;2](https://doi.org/10.1175/1520-0469(1971)028<0325:TOACIT>2.0.CO;2).
- Petoukhov, V., S. Rahmstorf, S. Petri, and H. J. Schellnhuber, 2013: Quasiresonant amplification of planetary waves and recent Northern Hemisphere weather extremes. *Proc. Natl. Acad. Sci. USA*, **110**, 5336–5341, doi:[10.1073/pnas.1222000110](https://doi.org/10.1073/pnas.1222000110).
- Ralph, F., and M. D. Dettinger, 2012: Historical and national perspectives on extreme West Coast precipitation associated with atmospheric rivers during December 2010. *Bull. Amer. Meteor. Soc.*, **93**, 783–790, doi:[10.1175/BAMS-D-11-00188.1](https://doi.org/10.1175/BAMS-D-11-00188.1).
- , P. Neiman, and G. Wick, 2004: Satellite and CALJET aircraft observations of atmospheric rivers over the eastern North Pacific Ocean during the winter of 1997/98. *Mon. Wea. Rev.*, **132**, 1721–1745, doi:[10.1175/1520-0493\(2004\)132<1721:SACAOO>2.0.CO;2](https://doi.org/10.1175/1520-0493(2004)132<1721:SACAOO>2.0.CO;2).
- , —, and R. Rotunno, 2005: Dropsonde observations in low-level jets over the northeastern Pacific Ocean from CALJET-1998 and PACJET-2001: Mean vertical-profile and atmospheric-river characteristics. *Mon. Wea. Rev.*, **133**, 889–910, doi:[10.1175/MWR2896.1](https://doi.org/10.1175/MWR2896.1).
- , —, G. Wick, S. I. Gutman, M. D. Dettinger, D. R. Cayan, and A. B. White, 2006: Flooding on California's Russian River: Role of atmospheric rivers. *Geophys. Res. Lett.*, **33**, 3–7, doi:[10.1029/2006GL026689](https://doi.org/10.1029/2006GL026689).
- , —, G. Kiladis, K. Weickmann, and D. Reynolds, 2011: A multiscale observational case study of a Pacific atmospheric river exhibiting tropical–extratropical connections and a mesoscale frontal wave. *Mon. Wea. Rev.*, **139**, 1169–1189, doi:[10.1175/2010MWR3596.1](https://doi.org/10.1175/2010MWR3596.1).
- Reynolds, R. W., T. M. Smith, C. Liu, D. B. Chelton, K. S. Casey, and M. G. Schlax, 2007: Daily high-resolution-blended analyses for sea surface temperature. *J. Climate*, **20**, 5473–5496, doi:[10.1175/2007JCLI1824.1](https://doi.org/10.1175/2007JCLI1824.1).
- Skamarock, W. C., J. B. Klemp, J. Dudhia, D. O. Gill, D. M. Barker, W. Wang, and J. G. Powers, 2005: A description of the advanced research WRF version 2. NCAR Tech. Note NCAR/TN-468+STR, 88 pp. [Available online at http://www.mmm.ucar.edu/wrf/users/docs/arw_v2.pdf.]
- Smith, B., S. Yuter, P. Neiman, and D. Kingsmill, 2010: Water vapor fluxes and orographic precipitation over northern California associated with a landfalling atmospheric river. *Mon. Wea. Rev.*, **138**, 74–100, doi:[10.1175/2009MWR2939.1](https://doi.org/10.1175/2009MWR2939.1).
- Sodemann, H., and A. Stohl, 2013: Moisture origin and meridional transport in atmospheric rivers and their association with multiple cyclones. *Mon. Wea. Rev.*, **141**, 2850–2868, doi:[10.1175/MWR-D-12-00256.1](https://doi.org/10.1175/MWR-D-12-00256.1).
- Trenberth, K. E., A. Dai, R. M. Rasmussen, and D. B. Parsons, 2003: The changing character of precipitation. *Bull. Amer. Meteor. Soc.*, **84**, 1205–1217, doi:[10.1175/BAMS-84-9-1205](https://doi.org/10.1175/BAMS-84-9-1205).
- Witze, A., 2015: CalWater 2015 targets atmospheric rivers off California. *Nature*, **517**, 424–425, doi:[10.1038/517424a](https://doi.org/10.1038/517424a).
- Wu, Y., M. Ting, R. Seager, H.-P. Huang, and M. A. Cane, 2011: Changes in storm tracks and energy transports in a warmer climate simulated by the GFDL CM2.1 model. *Climate Dyn.*, **37**, 53–72, doi:[10.1007/s00382-010-0776-4](https://doi.org/10.1007/s00382-010-0776-4).
- Zhu, Y., and R. Newell, 1998: A proposed algorithm for moisture fluxes from atmospheric rivers. *Mon. Wea. Rev.*, **126**, 725–735, doi:[10.1175/1520-0493\(1998\)126<0725:APAFMF>2.0.CO;2](https://doi.org/10.1175/1520-0493(1998)126<0725:APAFMF>2.0.CO;2).